Ultramicroscopy 148 (2015) 94–104

Contents lists available at ScienceDirect

Ultramicroscopy

journal homepage: www.elsevier.com/locate/ultramic

Designing a standard for strain mapping: HR-EBSD analysis of SiGe thin film structures on Si

M.D. Vaudin [a,*], W.A. Osborn [a], L.H. Friedman [a], J.M. Gorham [a], V. Vartanian [b], R.F. Cook [a]

[a] Materials Measurement Science Division, National Institute of Standards and Technology, Gaithersburg, MD 20899, USA
[b] 3D Interconnect Division, SEMATECH, Albany, NY 12203, USA

ARTICLE INFO

Article history:
Received 11 July 2014
Received in revised form
16 September 2014
Accepted 21 September 2014
Available online 30 September 2014

Keywords:
Electron backscattered diffraction
EBSD
Epitaxial SiGe–Si
Strain measurement
Standard

ABSTRACT

Patterned SiGe thin film structures, heteroepitaxially deposited on Si substrates, are investigated as potential reference standards to establish the accuracy of high resolution electron backscattered diffraction (HR-EBSD) strain measurement methods. The proposed standards incorporate thin films of tetragonally distorted epitaxial $Si_{1-x}Ge_x$ adjacent to strain-free Si. Six films of three different nominal compositions (x=0.2, 0.3, and 0.4) and various thicknesses were studied. Film composition and out-of-plane lattice spacing measurements, by x-ray photoelectron spectroscopy and x-ray diffraction, respectively, provided independent determinations of film epitaxy and predictions of tetragonal strain for direct comparison with HR-EBSD strain measurements. Films assessed to be coherent with the substrate exhibited tetragonal strain values measured by HR-EBSD identical to those predicted from the composition and x-ray diffraction measurements, within experimental relative uncertainties of order 2%. Such films thus provide suitable prototypes for designing a strain reference standard.

Published by Elsevier B.V.

1. Introduction

High resolution electron backscattered diffraction (HR-EBSD) is a rapidly evolving technique for measuring lattice strains and rotations with great spatial resolution; see reviews of [1,2]. The technique thus has potential for broad application in the development and manufacturing of small-scale devices in which engineered strain must be controlled to optimize device performance [3]. For example, deliberately incorporated stress is used to tune the mechanical responses of components in microelectromechanical and nanoelectromechanical systems [4], the electrical responses of complementary metal–oxide–semiconductor structures [3,5], and the optical responses of nanostructures and metamaterials, [3,6]. HR-EBSD also has potential for identifying unintended strains that limit device reliability, for example, the strains associated with cracks, dislocations, or other microstructural features [7,8] that can cause component failure. The technique can be applied to a broad range of materials, including metals and ceramics, although, because of the technological applications noted above, most attention has focused on semiconductors [1,2].

HR-EBSD is performed in a scanning electron microscope (SEM) and (as shown here and elsewhere [9,10]) is capable of strain measurement precision—the distribution of repeated measurements about a mean strain value—of approximately 10^{-4}, and perhaps much better (4×10^{-7} [11,12]) at (lateral) spatial resolutions of a few tens of nanometers [13]. However, the accuracy of the technique—how closely mean strain values estimate the true value—has not been thoroughly investigated, although it was of concern from the earliest demonstrations: Troost et al. [14] compared HR-EBSD measurements of the out-of-plane strain of silicon-germanium (SiGe) films, heteroepitaxially deposited on silicon (Si) substrates, with independent high-resolution x-ray-diffraction (HR-XRD) measurements and showed agreement to within about 10^{-3}. Wilkinson, [9] performed similar HR-EBSD measurements on SiGe–Si structures and using the XRD measurements of Bowen et al. [15] demonstrated agreement to within about 2×10^{-4}. Villert et al. [10] compared HR-EBSD measurements of components of the full strain tensor with those predicted from finite element analyses (FEA) of loaded Si beams and SiGe pads on Si substrates and showed agreement to within about 10^{-4} and 10^{-3}, respectively. Villert et al. also compared strains determined using HR-EBSD analysis methods applied to simulated strained Cu diffraction patterns and suggested an accuracy of 3.5×10^{-5} was possible. Encouraging as these results are, users of the technique have found that strain values determined by HR-EBSD on a given structure or component depend on selection

* Corresponding author.
E-mail address: mark.vaudin@nist.gov (M.D. Vaudin).

http://dx.doi.org/10.1016/j.ultramic.2014.09.007
0304-3991/Published by Elsevier B.V.

of many experimental and analysis parameters [10–13,16,17], rendering assessment of accuracy ambiguous. There is currently no standard or reference material that can be used to verify that a particular experimental setup and analysis method produces results that are accurate; a lack noted recently by Wilkinson [2] and Britton et al. [11]. The work reported here represents significant progress towards a NIST reference material (RM) that has a specified strain state traceable to the international system of units (the SI) *via* XRD. The planned RM will allow EBSD strain microscopy to be carried out in a standard EBSD-equipped SEM and the accuracy of the measurements established in a quantitative manner.

EBSD strain measurement is performed by collecting HR-EBSD patterns (EBSPs) from sample points and a reference point on a planar sample; the reference point is typically unstrained. Applying cross-correlation methods to pairs of reference and sample EBSPs allows the crystal lattices at the two points to be compared and lattice strain and rotation of the sample point determined relative to the reference point [9,13,14]. The RM artifacts investigated here are epitaxial films of silicon-germanium alloys ($Si_{1-x}Ge_x$) on Si substrates. Both $Si_{1-x}Ge_x$ and Si have the diamond-cubic lattice structure. Under conditions of epitaxy $Si_{1-x}Ge_x$ films are tetragonally deformed with equibiaxial compressive strain in the plane of the film and tensile strain normal to the film. The $Si_{1-x}Ge_x$ films are patterned to form near-planar structures and HR-EBSD is used to measure the strain tensor at sample points on the structures using the Si substrate for a reference point. The use of $Si_{1-x}Ge_x$ films has advantages over other material systems: the lattice spacings of Si (0.5431 nm) and Ge (0.5657 nm) differ by 4.2% [18], and the lattice spacing relationship for $Si_{1-x}Ge_x$ alloys as a function of composition is well-characterized and approximately linear in composition, x [19]; epitaxial deposition of $Si_{1-x}Ge_x$ on Si is a commercialized process and films can be grown with strains up to 2% that are stable or metastable [3,5]; and, significant work on the thermodynamics and kinetics of misfit dislocation generation in $Si_{1-x}Ge_x$ thin films and the effect on epitaxy and critical thickness has been carried out by Houghton et al. [20,21] among others, so that relatively reliable *a priori* predictions of thickness and composition combinations that maintain perfect epitaxy can be made. Finally, there have been many prior demonstrations of HR-EBSD-based strain measurements of $Si_{1-x}Ge_x$-on-Si structures, primarily by Wilkinson et al. [9,10,13,14,16,22,23].

A variety of thicknesses and compositions of patterned $Si_{1-x}Ge_x$ films are studied here, with a view to establishing thickness and composition bounds for a RM suitable as a strain calibration artifact for a variety of microscopy techniques in addition to EBSD (*e.g.*, confocal Raman microscopy [24–27] or micro-beam XRD [28]). Critical extensions to the previous observations are the use of x-ray photoelectron spectroscopy (XPS) as an independent measure of film composition—as this determines the unstrained $Si_{1-x}Ge_x$ lattice parameter and elastic constants—and the use of XRD as an independent measure of film strain—as this provides a measure of the degree of epitaxy if the composition is known. A further check on the film thickness and degree of epitaxy is provided by x-ray reflectivity (XRR). The next section describes the RM prototype and the experimental methods used. This is followed by a description of the analysis and parameters used to inter-relate the various measures of strain determined by the experimental measurements. The measurement results are then presented; discussion of these results focuses on the selection of an optimized film structure and the next steps required to establish a workable microscopy strain standard.

2. Material and experimental methods

2.1. Sample fabrication procedure

The samples used in this study included both blanket and patterned films on Si substrates. Blanket $Si_{1-x}Ge_x$ films were deposited heteroepitaxially on 300 mm Si (001) wafers using commercial processes at three compositions, x; nominally $x=0.2$, 0.3, and 0.4. To separate composition and strain effects, two thicknesses, t, were grown at each composition for nominally coherent states (thin films, tens of nanometers thick) and relaxed states (thick films, hundreds of nanometers thick). To prevent non-uniform oxidation of $Si_{1-x}Ge_x$ [29,30], very thin (≈ 1.5 nm thick) Si capping layers were grown on top of the $Si_{1-x}Ge_x$ layers, allowing the native oxide of Si, SiO_2, to form as an overlayer, without altering Ge compositional uniformity near the surface. The films were designated by their nominal (t, x) doublet, *e.g.*, (50 nm, 0.2); the six samples studied are listed in Table 1. Chips, 25 mm × 25 mm, were diced from each of the six unique wafers; photoresist was then deposited on the chips and patterned using photolithographic mask, exposure, and developing processes. The photoresist pattern was then used as a mask and the exposed $Si_{1-x}Ge_x$ film removed by etching using a $Cl_2+SiCl_4+N_2$ plasma process and optical endpoint spectroscopy to terminate etching when the intensity of the 265 nm Ge line in the plasma decreased to background [31]. Refinement of the etching process was critical to achieving termination at the $Si_{1-x}Ge_x$–Si interface, without overetching the Si substrate, and enabling subsequent clean removal of the photoresist without contamination. After $Si_{1-x}Ge_x$ etching, the photoresist was removed using solvent and a low power O_2 plasma descum process. Chips from each of the wafers were also retained in pristine blanket form. XRD measurements were performed on both the pristine blankets and processed chips (see Section 2.3) and the results compared to ensure that no unintentional modification of the films had occurred during microfabrication [31].

Table 1
Dimensions, compositions, and deformation states of $Si_{1-x}Ge_x$ films on Si substrates.

Sample label	Thickness, t (nm)	Composition[a], x (Ge at%)	Lattice spacing ratio[a], $(r-1)$ (10^{-2})	Film–substrate coherency[a], η	Predicted tetragonal distortion[a], ε_T^{pre} (10^{-2})	Measured tetragonal distortion[b], ε_T^{EBSD} (10^{-2})
(50 nm, 0.2)	47.4 (XRR)	19.4 ± 0.2	1.28 ± 0.01	0.977 ± 0.046	1.25 ± 0.04	1.23 ± 0.02
(35 nm, 0.3)	35.9 (XRR)	27.9 ± 0.3	1.91 ± 0.01	1.036 ± 0.042	1.93 ± 0.05	1.92 ± 0.03
(40 nm, 0.4)	59.3 (SEM)	40.0 ± 0.4	2.25 ± 0.01	0.588 ± 0.030	1.59 ± 0.06	1.15 ± 0.15
(500 nm, 0.2)	445 (SEM)	19.6 ± 0.2	0.83 ± 0.01	0.157 ± 0.035	0.20 ± 0.04	0.32 ± 0.06
(800 nm, 0.3)	791 (SEM)	29.9 ± 1.1	1.28 ± 0.01	0.153 ± 0.066	0.31 ± 0.12	0.03 ± 0.06
(200 nm, 0.4)	158 (SEM)	41.5 ± 1.0	1.79 ± 0.01	0.141 ± 0.045	0.40 ± 0.12	0.02 ± 0.11

[a] Uncertainties represent one standard deviation of the mean value, determined from repeated experimental measurements and propagation of variance when required.
[b] Uncertainties represent one standard deviation of repeated experimental measurements.

The pattern formed on the chips of each film type was identical, shown in the schematic diagram of Fig. 1. The major feature of the pattern, in the upper portion of the diagram, is a 20 mm × 12 mm pad of $Si_{1-x}Ge_x$ designed for XRD, XRR, and XPS measurements. In the lower left of the diagram is a series of standard gratings: 10 mm long stripes of $Si_{1-x}Ge_x$ standing films with widths from 1 μm to 50 μm separated by Si substrate gaps the same width as the stripes. These stripes are particularly suited for HR-EBSD measurements as the wider stripes (10 μm and wider) attained invariant strain levels in their centers; the narrower stripes can be used for investigation of edge effects by EBSD and other microscopy techniques and are not investigated here. In the lower right of the diagram are a series of fine features: narrow gratings, annuli, checkerboards, and a starburst. These features have more complicated strain states than the long stripes and are also not investigated here. A SEM image of the end of a 50 μm stripe is shown in Fig. 2, along with the coordinate system to be used in the strain analysis. Cross-section images were used to determine the thickness of the $Si_{1-x}Ge_x$ films from SEM measurements of cleaved blanket-film chips using a mixture of backscattered and secondary electrons to image the Si-$Si_{1-x}Ge_x$ interface; such measurements for four of the six films are given in Table 1. XRR thickness measurements were used for the two thinnest films, see Table 1.

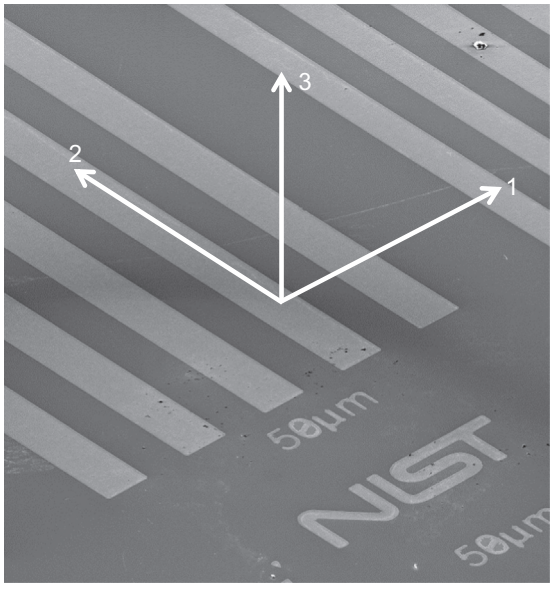

Fig. 2. SEM image of the end of a 50 μm wide × 50 nm thick $Si_{1-x}Ge_x$ stripe on a Si substrate. The coordinate system for strain measurement is indicated.

2.2. XPS measurement method

XPS was used to measure film composition for each of the unique $Si_{1-x}Ge_x$ wafers using a typical depth-profiling sputtering procedure. All measurements were performed on an Axis DLD Ultra Imaging X-ray Photoelectron Spectrometer (Kratos Analytical, Spring Valley, NY) [32]. For each wafer, one of the chips without any etched features (a so-called blanket film sample) was mounted onto an azimuthal stage, loaded into the analysis chamber with a base pressure $< 1.3 \times 10^{-7}$ Pa (10^{-9} Torr), and aligned by optical microscopy. All spectra were acquired using a monochromatic Al K_α x-ray source operating at 150 W (10 mA; 15 kV) and an analysis spot with a diameter ≈225 μm. A hemispherical analyzer using a pass energy of 160 eV (2.6×10^{-17} J) was used to collect spectra from the Ge (2p), O (1s), C (1s), Si (2p), and Ge (3d) regions in 0.1 eV/step increments. These elemental regions were collected after each sputter increment, and additional wide surveys were collected before the first and after the last sputter increment to ensure surface uniformity.

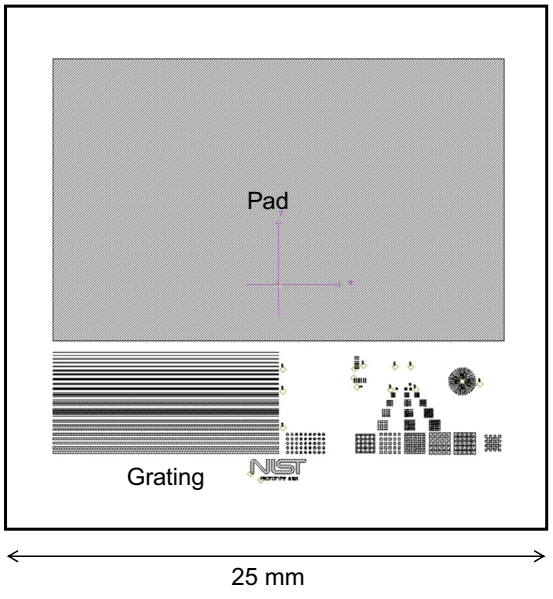

Fig. 1. Schematic plan diagram of the prototype NIST strain artifact RM. The 25 mm square chip contains thin-film $Si_{1-x}Ge_x$ surface structures heteroepitaxially deposited on a (001) Si substrate to form lattices of specified $Si_{1-x}Ge_x$ strain relative to the Si reference. The chip and pad edges and grating axes are aligned along ⟨110⟩ directions.

Depth profiling was accomplished using 45° incident 2 keV argon (Ar) ions generated using a floating ion gun with an extractor current of 70 μA. Prior to starting a set of experiments, the Ar supply line was depressurized using a mechanical pump to less than 4.0×10^{-3} Torr and repressurized. Throughout the depth profile, the Ar gas and ion gun filament remained on to maximize uniformity and minimize contamination. After completion of a sputter increment, the ion gun accelerating voltage was turned off to stop Ar ion beam bombardment. An 1800 s delay was inserted after every sputter increment to stabilize the surface prior to the acquisition of spectra. The pressure in the analysis chamber during sputtering and spectra acquisition was between 2.7×10^{-6} Pa (2.0×10^{-8} Torr) and 6.7×10^{-6} Pa (5.0×10^{-8} Torr).

Data analysis was conducted using CasaXPS software (Teignmouth, UK) for the Si (2p) and the Ge (3d) spectral regions, which were fit with a Shirley background and an average endpoint width of 5. Peak positions were not adjusted or corrected for minor shifts in binding energy and intensities are reported as measured. Atomic relative sensitivity factors (aRSFs) were calculated based on equations from the literature using pure elemental samples of Si and Ge as references and correcting for the atomic density portion of matrix effects [33]. Atomic densities were determined by lattice constants experimentally derived in previous studies [19]. The $aRSF^{Ge}$ was determined to be 1.8178 ± 0.0093 (relative to $aRSF^{Si} = 1$). The uncertainty in aRSF is reported as plus and minus one standard deviation based on Monte Carlo simulations of counting statistics (Casa XPS) combined with reported uncertainty of the lattice constants [19]. Mean values of the Ge composition were calculated based on measurements in the plateau regions of the depth profiles (> six points of analysis/profile) for Si and Ge only. The uncertainties associated with the composition values combine the uncertainties (standard deviations) of the mean values and the aRSF uncertainty noted above.

2.3. X-ray measurement methods

For each sample, the Si 004 peak at an XRD angle of $2\theta \approx 69.15^\circ$ and the adjacent $Si_{1-x}Ge_x$ 004 peak were measured over the range $66^\circ < 2\theta < 71^\circ$ in a single scan using Cu K_α radiation in a conventional powder diffractometer (Siemens D500) equipped with a Johansson optic (Ge monochromator) and a sample changer. (Note that a Ge 004 peak would be at $2\theta \approx 66.02^\circ$ and no such peak was observed for any film). Peak positions were determined using conventional analysis techniques and the ratio of the (004) plane spacings in the film and substrate were calculated by applying Bragg's law, providing the most accurate and traceable measurement of the spacings of planes parallel to the sample surface. Experimental conditions were optimized so that the details of diffraction features over nearly five orders of magnitude of intensity could be resolved; in particular dwell times of up to 70 s were used in the collection of high resolution scans.

XRR measurements were employed to measure the film thickness for samples (50 nm, 0.2) and (35 nm, 0.3) using a Bruker (Madison, WI) D8 diffractometer. Measurements were made over a scattering angle range of 0°–4° and were analyzed using the Leptos software package (Bruker). The model for the sample consisted of Si substrate, $Si_{1-x}Ge_x$ film, and SiO_2 surface layer. XRD spectra for these samples were also analyzed using the Leptos software to determine film thickness.

2.4. EBSD measurement method

High resolution EBSPs were collected using a commercial EBSD system (Oxford HKL Nordlys II, Abingdon, UK) installed on a cold tip field-emission gun SEM (Hitachi model 4700, Japan), typically operated at an accelerating voltage of 20 kV with a probe current measured by Faraday cup of about 2 nA. Referring to the coordinate axes in Fig. 2, the untilted samples were adjusted so that the stripes (as seen in Figs. 1 and 2) were parallel to the vertical (or 2-) axis of the SEM detector screen; it was assumed that the sample and detector 1-axes were parallel. The sample was then rotated about this 1-axis so that the sample and detector normals (3-axes) were related by a rotation of 20° about their parallel 1-axes; the electron beam was parallel to the vertical (or 2-) axis of the detector and 70° to the 3-axis of the sample. Line scans in the 1-direction were collected from each sample, with scans extending across several (10, 20, 30, 40, and 50) μm $Si_{1-x}Ge_x$ stripes. Typically, the scans consisted of 250–300 points with step sizes of 1 μm. EBSPs collected at each point were 1344 pixels × 1024 pixels with 8 bit intensity resolution; integration times were about 1 s/point. The image processing applied to each EBSP was image division by the background and contrast optimization. The background was recorded by demagnifying the SEM image to 50 × at which point the recorded diffraction background was featureless, as needed. A reference pattern was taken at the beginning of the line scan in a bare Si region away from the $Si_{1-x}Ge_x$ stripes and was frequently one of the first five patterns at the start of the scan. The pixel size for the EBSD detector used in these measurements is about 25 μm square. The cross-correlation method can measure EBSP shifts down to 0.05 pixels, and the distance from the sample to the detector was of the order of 500 pixels. Thus, as a rule of thumb we can calculate changes in EBSP orientation of the order of $0.05/500 = 10^{-4}$ rad as discussed by Britton et al. [11].

Analysis of the EBSPs was carried out using the CrossCourt software package (version 3.1, BLG Productions, Bristol, UK). CrossCourt uses Fourier cross-correlation methods to calculate eight of the nine components of the displacement gradient tensor, A_{ij}, at each point in the scan, where $A_{ij} = \partial u_i/\partial x_j$, u_i and x_j are displacement and position vectors, respectively, in the deformed material, and $(i, j) = (1, 2, 3)$. Several regions of interest (ROIs) are selected in the sample EBSP and cross-correlated with the same ROIs in the reference EBSP to determine the best-fit set of eight A_{ij} components describing the lattice transformation at the sample point. The method is sensitive to lattice orientation, dimension ratios, and shears, but does not sense dilatation; only the differences $A_{11} - A_{33}$ and $A_{22} - A_{33}$ are determined. A closure condition is applied to separate the three normal components; the condition used was that the surface normal traction was zero. In this case, the EBSPs were first cropped on the sides by 160 pixels to make an EBSP 1024 pixels square. Twenty one ROIs, 256 × 256 pixels square, were then selected, one centered on the EBSP at pixel (512, 512) and 20 centered on a circle of radius 384 pixels also centered at (512, 512). Prior to cross-correlation, a band-pass filter was applied in the Fourier domain to reduce the effects of noise and intensity variations and improve the precision of peak location in the cross-correlation function; the filter was set to pass wavelengths in the range of 12.8–128 pixels. From the components of A_{ij}, normal strains, shear strains, and lattice rotations can be determined. In particular, of interest here, the infinitesimal strain tensor is given by the symmetric component of A_{ij}, $\varepsilon_{ij} = (A_{ij} + A_{ji})/2$. As the measurements here used the cubic Si lattice as a reference point, the strains determined by EBSD, ε_{ij}^{EBSD}, for sample points on the stripes, can be used to determine the tetragonality of the epitaxial $Si_{1-x}Ge_x$, as discussed in the next section.

3. Analytical framework

This section provides an analysis for the predicted tetragonal distortion of a $Si_{1-x}Ge_x$ film from XRD lattice parameter measurements, for direct comparison with that determined from EBSD strain measurements. A critical component of the analysis is the relationship between the distortion predicted by XRD, determined relative to an unstressed $Si_{1-x}Ge_x$ alloy, with that measured by EBSD, determined relative to an unstrained Si lattice reference point. The analysis uses established variations in the lattice parameter and elastic constants with composition [19,34,35] for $Si_{1-x}Ge_x$ and, in addition to the distortion prediction, provides a means of assessing the degree of coherency of the $Si_{1-x}Ge_x$ film epitaxy on the Si substrate.

The addition of Ge to Si to form a random solid-solution alloy leads to an unconstrained volume expansion (dilatation) of the diamond cubic $Si_{1-x}Ge_x$ lattice relative to that of Si. The equilibrium lattice spacing of $Si_{1-x}Ge_x$, $a_{SiGe}(x)$, as a function of composition is given by

$$a_{SiGe}(x) = (1 + 0.0365x + 0.0052x^2)a_{Si}, \quad (1)$$

where a_{Si} is the lattice spacing of Si and x is composition. The coefficients in Eq. (1) were determined by the least-squares best-fit to the tabulated lattice constants of $Si_{1-x}Ge_x$ from Dismukes et al. [19] and have uncertainties of approximately 2×10^{-4}. The solid solution dilatation of $Si_{1-x}Ge_x$ relative to Si is given by $3a_{SiGe}(x)/a_{Si} > 1$, shown in the upper schematic diagram of Fig. 3 (a), in which $Si_{1-x}Ge_x$ is in its unstressed or (fully) relaxed state. In this state, an interface between $Si_{1-x}Ge_x$ and Si is completely incoherent, shown in the lower schematic diagram of Fig. 3(a). The mismatch strain, $\varepsilon_m(x)$, between $Si_{1-x}Ge_x$ in this state and Si, relative to unstrained $Si_{1-x}Ge_x$, is

$$\varepsilon_m(x) = \frac{a_{Si} - a_{SiGe}(x)}{a_{SiGe}(x)}, \quad (2)$$

and $\varepsilon_m(x) < 0$.

If a $Si_{1-x}Ge_x$ film is epitaxially deposited on a Si substrate with perfect coherency, and the film is very thin such that the substrate is undeformed, the $Si_{1-x}Ge_x$ is tetragonally distorted, as shown in

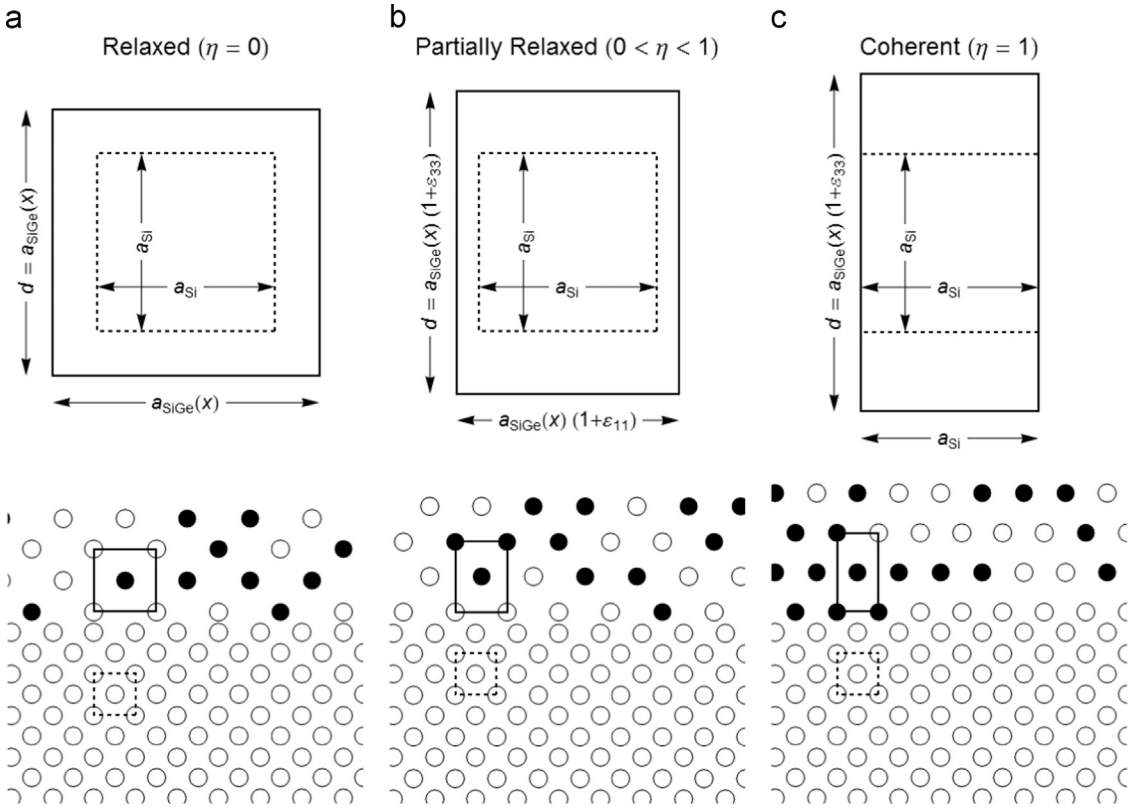

Fig. 3. Schematic diagrams of $Si_{1-x}Ge_x$ films epitaxially deposited on (001) Si substrates. Lower diagrams represent elevations of the common (100) planes; open circles represent Si, closed circles represent Ge. The diamond-cubic unit cell outlines are shown as solid lines in the $Si_{1-x}Ge_x$ and dashed lines in the Si. Upper diagrams show expanded outlines of the unit cells, along with cell dimensions in terms of lattice spacings of the relaxed structures and epitaxial strains. (a) A fully relaxed, cubic $Si_{1-x}Ge_x$ film, (b) a partially relaxed, tetragonal $Si_{1-x}Ge_x$ film, and (c) a fully coherent, maximally tetragonal $Si_{1-x}Ge_x$ film.

Fig. 3(c). The in-plane (∥) strain in the film parallel to the interface is then equibiaxial and given by (using the coordinate system of Fig. 2)

$$\varepsilon_{11} = \varepsilon_{22} = \varepsilon_{||} = \varepsilon_m(x), \tag{3}$$

and the in-plane $Si_{1-x}Ge_x$ lattice spacing is $a_{||} = [1+\varepsilon_m(x)]a_{SiGe}(x) = a_{Si}$. The out-of-plane (⊥) strain perpendicular to the interface is given by

$$\varepsilon_{33} = \varepsilon_{\perp} = \frac{d - a_{SiGe}(x)}{a_{SiGe}(x)}, \tag{4}$$

where d is the out-of-plane $Si_{1-x}Ge_x$ lattice spacing. The relationship between the strains of Eqs. (3) and (4) is found from mechanical equilibrium:

$$\sigma_{33} = \sigma_{\perp} = C_{11}(x)\varepsilon_{\perp} + 2C_{12}(x)\varepsilon_{||} = 0, \tag{5}$$

such that

$$\varepsilon_{\perp} = -\frac{2C_{12}(x)}{C_{11}(x)}\varepsilon_{||} \tag{6}$$

and $C_{11}(x)$ and $C_{12}(x)$ are (composition-dependent) elastic constants of $Si_{1-x}Ge_x$ (in contracted notation). Although C_{11} and C_{12} are functions of composition, the ratio $2C_{12}(x)/C_{11}(x)$ is a slowly varying function of x; over the x range from 0.0 to 0.4, $2C_{12}(x)/C_{11}(x)$ varies linearly from 0.772 to 0.764 (*i.e.* 0.5% relative) which demonstrates the slowly varying nature. A perfectly coherent film is thus in a triaxial strain state with in-plane equibiaxial compression and out-of-plane expansion.

The elastic strain energy density of a film may be decreased by misfit dislocations at or near the Si–$Si_{1-x}Ge_x$ interface, partially or fully eliminating the $Si_{1-x}Ge_x$ epitaxial strain and reducing the coherency. It is useful to define a coherency factor, η, which varies from zero, for fully relaxed films (Fig. 3(a)) with $a_{||} = a_{SiGe}(x)$, to one, for fully coherent dislocation-free films (Fig. 3(c)) with $a_{||} = a_{Si}$:

$$\eta = \frac{a_{||} - a_{SiGe}(x)}{a_{Si} - a_{SiGe}(x)}. \tag{7}$$

For partially relaxed films the strains are modified by η as a multiplicative factor, so that the strain components of Eqs. (3) and (4) are given generally as

$$\varepsilon_{11} = \varepsilon_{22} = \eta\varepsilon_m(x) \tag{8}$$

and

$$\varepsilon_{33} = -\eta\frac{2C_{12}(x)}{C_{11}(x)}\varepsilon_m(x). \tag{9}$$

Fig. 3(b) is a schematic diagram of a partially relaxed film with $0 < \eta < 1$; the magnitudes of both strain components are decreased from that of Fig. 3(c) and the interface is only partially coherent (the core of single partial dislocation in the simplified two-dimensional diagram is visible).

The tetragonal distortion, ε_T, of the film relative to an unstrained $Si_{1-x}Ge_x$ lattice is given by the difference between Eqs. (8) and (9):

$$\varepsilon_T = \varepsilon_{33} - \varepsilon_{11} = \varepsilon_{33} - \varepsilon_{22} = -\varepsilon_m(x)\left(1 + \frac{2C_{12}(x)}{C_{11}(x)}\right)\eta, \tag{10}$$

and is the product of terms that describe relaxed $Si_{1-x}Ge_x$, calculable from knowledge of the composition, x, alone and a term describing the degree of coherence with Si substrate, η, determinable from XRD measurements. XRD measurements can determine the ratio, r, of the out-of-plane lattice spacings for the $Si_{1-x}Ge_x$ film and the Si substrate. In particular, the (004) lattice

spacings were measured here, such that the ratio is given by $r=a_{SiGe}(004)/a_{Si}(004)$. Recognizing that the equilibrium relation of Eq. (6) is independent of the coherence state of the film gives a relationship between the in-plane and out-of-plane lattice spacings of $Si_{1-x}Ge_x$, $[d-a_{SiGe}(x)]=-[2C_{12}(x)/C_{11}(x)][a_{||}-a_{SiGe}(x)]$. Substituting these equations into Eq. (7) and re-arranging provides an expression for the coherency factor determinable from composition and x-ray diffraction measurements:

$$\eta=-\frac{C_{11}(x)}{2C_{12}(x)}\frac{ra_{Si}-a_{SiGe}(x)}{a_{Si}-a_{SiGe}(x)}. \tag{11}$$

The coherency factor may be used to predict the tetragonal distortion measured by EBSD, ε_T^{pre}. EBSD strains are measured relative to the unstrained Si lattice, however, and the tetragonal distortion of Eq. (10) must be modified to reflect the change in reference state, $\varepsilon_T^{pre}=(a_{SiGe}/a_{Si})\varepsilon_T$. Combining this equation and Eqs. (2) and (10) leads to an expression for the predicted EBSD-measured tetragonal distortion:

$$\varepsilon_T^{pre}=\left(1+\frac{2C_{12}(x)}{C_{11}(x)}\right)\frac{a_{SiGe}(x)-a_{Si}}{a_{Si}}\eta \tag{12}$$

and, again, is the product of terms involving only composition and the coherency term.

The experimental scheme that uses this analysis, Eqs. (11) and (12) in particular, to assess the accuracy of HR-EBSD strain measurements is then as follows: composition, x, of the $Si_{1-x}Ge_x$ film test structure is determined, here by XPS, and the unstrained $Si_{1-x}Ge_x$ lattice spacing, $a_{SiGe}(x)$, determined from Eq. (1). The ratio of the out-of-plane lattice spacings for the film and substrate, r, is determined by XRD. The coherence factor of the film, η, is then determined using Eq. (11) and knowledge of the substrate lattice spacing, a_{Si}, and the film elastic constants, $C_{11}(x)$ and $C_{12}(x)$. The elastic constants were determined by linear interpolation of the tabulated elastic constants of Si and Ge from McSkimin and Andreatch [34,35]. All of these quantities are then used in Eq. (12) to predict the tetragonal distortion measurable by EBSD, ε_T^{pre}. HR-EBSD measurements are then performed to determine the strain components ε_{11}^{EBSD}, ε_{22}^{EBSD}, and $\varepsilon_{33}^{EBSD}$and the EBSD-measured tetragonal distortion, ε_T^{EBSD}:

$$\varepsilon_T^{EBSD}=\varepsilon_{33}^{EBSD}-(\varepsilon_{11}^{EBSD}+\varepsilon_{22}^{EBSD})/2. \tag{13}$$

The experimental strain result determined from the measured quantities in Eq. (13) can be compared directly with the prediction from the quantities in Eq. (12) obtained independently. There are two other points of direct comparison between assumed elements of the analysis and the measurements: (i) the in-plane film strain is assumed equibiaxial, *i.e.*, ε_{11}^{EBSD} should equal ε_{22}^{EBSD}. (ii) Each component of the film–substrate system has been treated as homogeneous and hence the measured and predicted distortions should be equal, independent of the degree of coherence, *i.e.*, ε_T^{EBSD}should equal ε_T^{pre} independent of η.

4. Results

4.1. XPS results

XPS depth profiling was used to measure the through-thickness compositions of the films, allowing both average composition and composition uniformity to be determined. Fig. 4(a) shows representative spectra observed through the thickness of the (40 nm, 0.4) film. Pristine surface spectra (0 s sputter time) show the expected Ge (3d) and Si (2p) transitions. The Si (2p) spectrum exhibits the sharp Si^0 peak consistent with diamond-cubic Si as well as the higher energy broad Si^{4+} peak associated with SiO_2 [36]. A higher-energy broad peak in the Ge (2p) scan was not

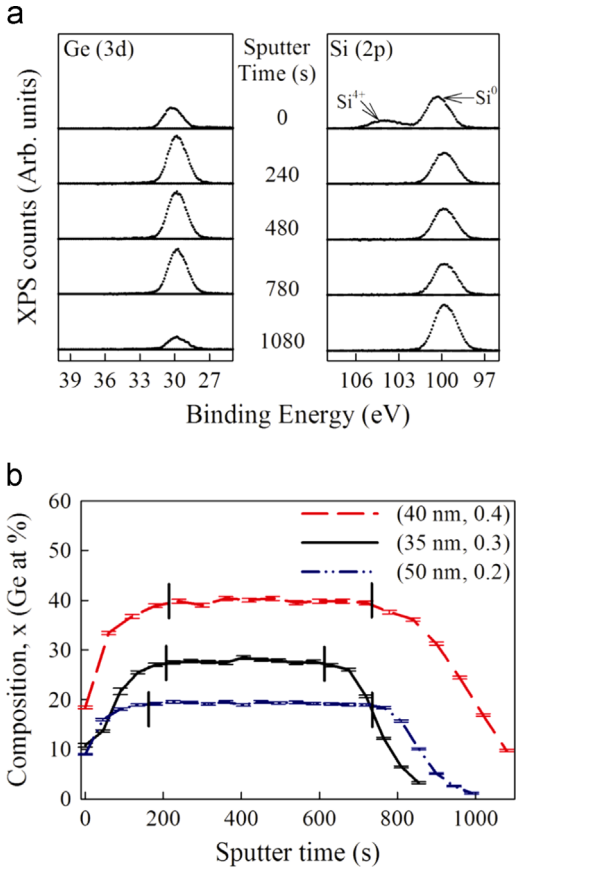

Fig. 4. (a) Selected regions of XPS spectra of $Si_{1-x}Ge_x$ films after various sputter times and (b) composition of $Si_{1-x}Ge_x$ films *vs.* sputter time for samples with nominal compositions of 0.2, 0.3, and 0.4 at% Ge. The plateaus in the composition values are indicative of invariant film compositions.

observed (data not shown), indicating that the Si cap layer did protect the $Si_{1-x}Ge_x$ film from oxidation. Scans of the O (1s) and C (1s) spectra (data not shown) indicated the presence of oxygen and carbon on the native Si oxide surface.

Once depth profiling began and the native surface oxide was removed, the Si (2p) and Ge (3d) spectra exhibited only Si^0 and Ge^0 peaks that were stable through the thickness of the film (240 s to 780 s cumulative sputter times in Fig. 4(a)). With additional sputtering, the sputtered surface neared the Si:$Si_{1-x}Ge_x$ heteroepitaxy interface and the Ge (3d) signal decreased in intensity relative to the Si (2p) signal (1080 s sputter time in Fig. 4(a)), until no Ge was detected. The relative intensities of the Si (2p) and Ge (3d) responses were analyzed as described above to determine the composition of the films as a function of sputtering time and therefore as a function of depth. The results of this procedure, to establish effective composition depth profiles, for the (50 nm, 0.2), (35 nm, 0.3), and (40 nm, 0.4) films is shown in Fig. 4(b); the Ge composition (x) increases as the sputtering surface proceeds through the SiO_2 capping layer, to a plateau as the surface proceeds through the $Si_{1-x}Ge_x$ film, and decreases to near zero as the surface enters the underlying Si substrate. The near invariant compositions observed in the plateau regions (indicated by the vertical lines) suggest composition uniformity of the $Si_{1-x}Ge_x$ films. To establish a composition for a film, a combined averaging and relative uncertainty analysis was applied to measurements contained within the plateau; this allowed the composition value to include uncertainties from individual analysis points and uncertainty from compositional non-uniformity through the film thickness. The composition values determined for all six films are given in Table 1; the measured values are all close to the nominal values.

4.2. XRD and XRR results

Fig. 5 shows diffraction patterns obtained from samples (50 nm, 0.2) and (35 nm, 0.3) using a logarithmic intensity scale. The 004 peaks from $Si_{1-x}Ge_x$ were well separated from the high intensity Si 004 peak, and application of Bragg's law to the peak positions gave the spacing ratios of planes parallel to the wafer, r. These values (as $r-1$) are given in Table 1. The sides of the $Si_{1-x}Ge_x$ peaks in Fig. 5 exhibited intensity oscillations caused by diffraction in the single crystal thin film. The existence of the oscillations suggests that these films were perfectly coherent with the Si substrate, and that the (004) plane spacing within each film was constant through the film. Similar scans obtained from samples (500 nm, 0.2), (800 nm, 0.3), (200 nm, 0.4), and (40 nm, 0.4) are shown in Fig. 6 and once again the $Si_{1-x}Ge_x$ and Si 004 peaks are well separated enabling r to be calculated, and these values are also given in Table 1. For these latter four samples, however, the $Si_{1-x}Ge_x$ 004 peaks exhibited no side oscillations, suggesting that these films contained lattice defects typical of partial coherence with the underlying Si substrate; misfit dislocations were partially accommodating the solid solution strain in these samples, leading to disorder in the films and extinction of the oscillations. (All six samples exhibited a small peak at a larger 2θ angle than the main Si 004 peak due to the Johansson optic allowing a small fraction of the $K\alpha_2$ component of the beam to pass through.) For each sample the Si and $Si_{1-x}Ge_x$ peaks were collected in the same scan, leading to very small uncertainty in the ratio r; repeated measurements involving remounting the samples showed that the measured ratios were repeatable to 1×10^{-4} and this is the uncertainty given in Table 1. The Si 004 peaks are not perfectly coincident in Figs. 5 and 6 due to small differences in sample mounting but the effect on the determined r values was insignificant.

The composition, x, was used to calculate the $Si_{1-x}Ge_x$ lattice spacing and elastic constants, which, along with the r value, were used to determine the coherency factor, η, for each film from Eq. (11). The η values are given in Table 1. The two films that exhibited side oscillations in the x-ray diffraction spectra (Fig. 5) had η values statistically identical to 1; that is, their lattice spacings were consistent with perfect coherency. The four films that did not exhibit side oscillations (Fig. 6) had η values significantly less than 1; their lattice spacings suggested only partial coherency. The lattice spacings, elastic constants, and coherency factors were then used to predict the tetragonal distortion measured by EBSD, ε_T^{pre}, for each film from Eq. (12). The ε_T^{pre} values are given in Table 1.

XRR data were collected from the samples in Fig. 5 to determine film thickness and the results are given in Table 1. In addition, the XRD oscillations in Fig. 5 were simulated and the film thickness parameter adjusted until the experimental and simulated oscillation positions coincided; there was no significant difference between the film thicknesses determined by XRR and XRD for these films. The XRR data from the films that were not perfectly coherent (Fig. 6) were of much lower quality and were not used for thickness estimation.

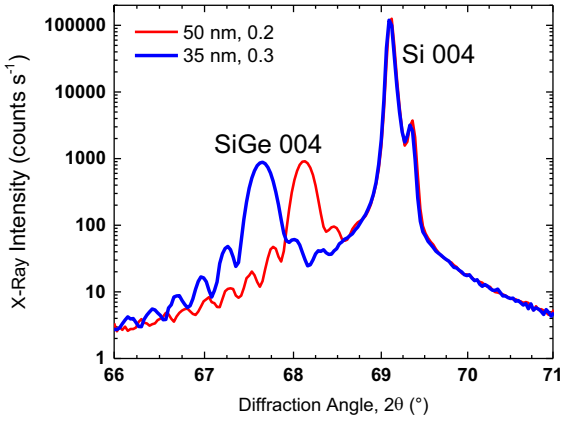

Fig. 5. XRD patterns from samples (35 nm, 0.3) and (50 nm, 0.2), plotted on a logarithmic scale, showing Si 004 and $Si_{1-x}Ge_x$ 004 peaks and single crystal $Si_{1-x}Ge_x$ oscillations.

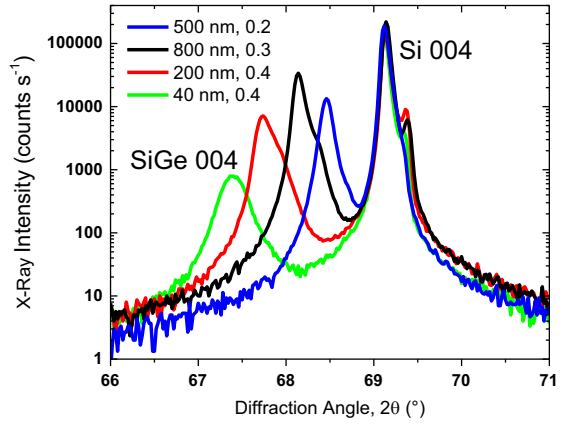

Fig. 6. XRD patterns from samples (500 nm, 0.2), (800 nm, 0.3), (40 nm, 0.4), and (200 nm, 0.4), plotted on a logarithmic scale, showing Si 004 and $Si_{1-x}Ge_x$ 004 peaks and the absence of $Si_{1-x}Ge_x$ single crystal oscillations.

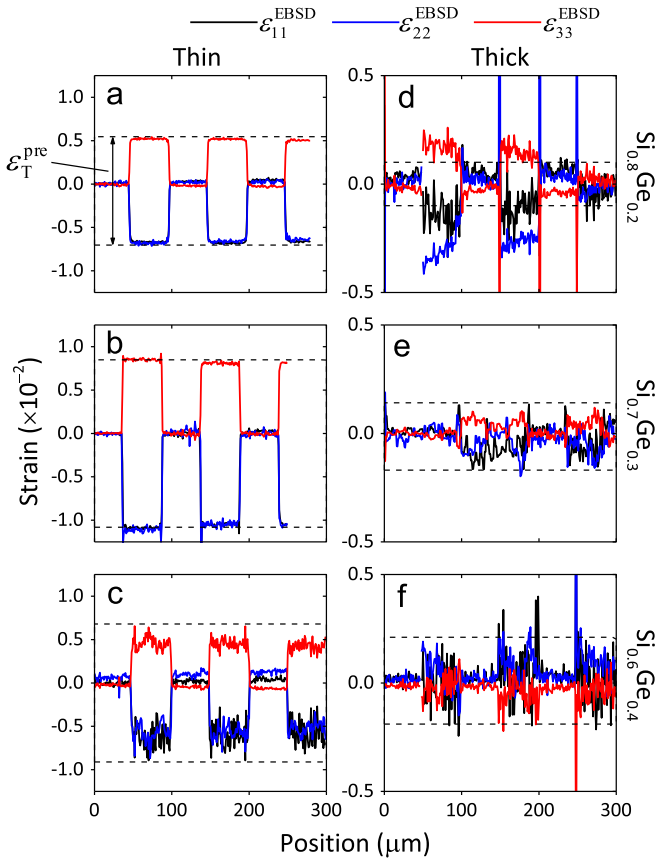

Fig. 7. EBSD line scans showing the normal strain components ε_{11}^{EBSD}, ε_{22}^{EBSD}, and ε_{33}^{EBSD} from thin samples (a) (50 nm, 0.2), (b) (35 nm, 0.3) and (c) (40 nm, 0.4), and thick samples (d) (200 nm, 0.4), (e) (800 nm, 0.3), and (f) (200 nm, 0.4). The magnitudes of the strain components are near zero in the Si gaps and have near-invariant values in the $Si_{1-x}Ge_x$ stripes. ε_T^{pre}, the predicted tetragonal strain, is indicated as the separation of the dashed lines.

4.3. EBSD results

Fig. 7 shows the results of line-scans across patterned 50 μm $Si_{1-x}Ge_x$ stripes and Si gaps for all six samples; the results are reported as EBSD measurements of the three normal strain components, ε_{11}^{EBSD}, ε_{22}^{EBSD}, and ε_{33}^{EBSD}. Each row represents a film of the same nominal composition, with Ge concentration, x, increasing from top to bottom. Each column represents films of similar thickness, with thickness, t, increasing from left to right. Measurements on (10, 20, 30, and 40) μm stripes gave identical results to those reported below.

The two films adjudged to have perfect coherency with the substrate, (50 nm, 0.2) and (35 nm, 0.3), top left in Fig. 7, exhibited the anticipated strain response. At position 0 μm, near the reference point location in the Si, all three strain components were zero. At the edge of the $Si_{1-x}Ge_x$ stripe there was an abrupt (one step) increase in the magnitude of the strain components: ε_{11}^{EBSD} and ε_{22}^{EBSD} becoming <0 and comparable in scale, reflecting the in-plane biaxial compression associated with heteroepitaxy of the $Si_{1-x}Ge_x$ on the smaller Si lattice; and ε_{33}^{EBSD} becoming >0 and approximately 80% of the magnitude of ε_{11}^{EBSD} or ε_{22}^{EBSD} (in agreement with Eq. (6)), reflecting the out-of-plane expansion associated with mechanical equilibrium of the film. The magnitudes of the strain components remained relatively constant over the width of the stripe before an abrupt decrease to zero strain at the gap edge; and then the pattern repeated. Comparison of the observations for these two films shows that the magnitudes of the strain components increased as the Ge composition increased from $x=0.2$ to $x=0.3$ (in agreement with Eqs. (1), (2), (3) and (6)). Finally, differences in the strain components within the $Si_{1-x}Ge_x$ stripes are in agreement with the tetragonal distortion predicted from the XPS composition and XRD lattice spacing measurements: the separations of the horizontal dashed lines in Fig. 7 represent the magnitudes of ε_T^{pre} (from Eqs. (11) and (12), see Table 1) and span the measured distortions, $\varepsilon_T^{EBSD}=\varepsilon_{33}^{EBSD}-\varepsilon_{11}^{EBSD}=\varepsilon_{33}^{EBSD}-\varepsilon_{22}^{EBSD}$ (Eq. (13)), for the fully coherent films almost identically.

The film judged to have partial coherency with the substrate, (40 nm, 0.4), bottom left in Fig. 7, exhibited close to the anticipated strain response. As above, there was near-zero strain in the Si gap, abrupt increases in the magnitudes of strain components at the stripe edges, and comparable scales for ε_{11}^{EBSD} and $\varepsilon_{22}^{EBSD}<0$ and ε_{33}^{EBSD} of opposite sign and about 80% of $|\varepsilon_{11}^{EBSD}|$ or $|\varepsilon_{22}^{EBSD}|$ within the stripes. There was, however, much greater variability in the strain components within the stripes than observed for the fully coherent films, and the span of the composition and XRD-predicted tetragonal distortion was greater than that measured by EBSD; the predicted distortion was already reduced from the maximum value for a film of this composition due to lack of coherence between the film and substrate (see Table 1). The films judged to have near-zero coherency with the substrate, (500 nm, 0.2), (800 nm, 0.3), and (200 nm, 0.4), right column in Fig. 7, exhibited extremely small and variable EBSD strain responses. In some cases the response observed in the coherent and partially coherent films was detectable, films (500 nm, 0.2) and (200 nm, 0.4), although the strain response in the stripes was extremely variable and in the case of (200 nm, 0.4) of the wrong sign. For the thickest film, however, (800 nm, 0.3), the response was not well correlated with the location of the stripes. For the three incoherent films, the already much-reduced predicted tetragonal distortion was comparable in scale, although somewhat larger, than that inferred from the extremely variable EBSD strain measurements. The increased variability in the EBSD response in the Si gaps for the partial- and zero-coherence film samples is believed to be due to surface topography associated with the etching process (etching hundreds of nanometers generates greater surface roughness than etching tens of nanometers).

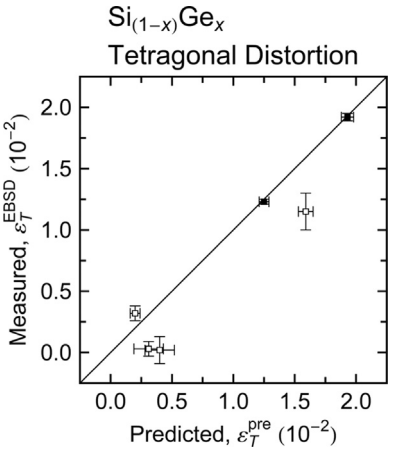

Fig. 8. Plot of the tetragonal distortion for $Si_{1-x}Ge_x$ films on Si substrates measured by EBSD against that predicted by XPS and XRD. Data and error bars are from Table 1. Filled squares represent "coherent films" shown in Fig. 5; open squares represent "incoherent films" shown in Fig. 6. The solid line indicates perfect agreement and is a guide to the eye.

To determine values of the tetragonal distortion measured by EBSD, ε_T^{EBSD}, a modified version of Eq. (13) was used:

$$\varepsilon_T^{EBSD}=\langle\varepsilon_{33}^{EBSD}-(\varepsilon_{11}^{EBSD}+\varepsilon_{22}^{EBSD})/2-\langle\varepsilon_{33}^{EBSD}\rangle_{Si}+\langle\varepsilon_{11}^{EBSD}\rangle_{Si}/2+\langle\varepsilon_{22}^{EBSD}\rangle_{Si}/2\rangle_{SiGe} \quad (14)$$

to take into account differences between ε_{11}^{EBSD} and ε_{22}^{EBSD} and local deviations from measured zero strain in the gaps; $\langle\ \rangle$ represent averages. Regions in each scan were identified that had well-defined Si gaps both sides of $Si_{1-x}Ge_x$ stripes. Twenty one observations of the normal strain components from both Si gaps adjacent to a stripe were averaged to obtain gap values of $\langle\varepsilon_{11}^{EBSD}\rangle_{Si}$, $\langle\varepsilon_{22}^{EBSD}\rangle_{Si}$, and $\langle\varepsilon_{33}^{EBSD}\rangle_{Si}$ (to set a local reference). Twenty one values of the normal strain components in the stripe were then selected, the local reference subtracted from each value to provide 21 estimates of the tetragonal distortion in the stripe, and the average of these estimates calculated using Eq. (14). Measurements for all stripes were then averaged to give the mean values of ε_T^{EBSD} for each film, given in Table 1. The standard deviations of the estimates of the tetragonal distortions for each film were also calculated and are given in Table 1. Fig. 8 is a plot of the tetragonal distortion for the $Si_{1-x}Ge_x$ films measured by EBSD against that predicted from composition and XRD measurements; the symbols represent the means and uncertainties from Table 1, the solid line indicates ideal agreement. The correlation between the measured and predicted values is strong, but only those films that were coherent with the Si substrate exhibited ideal agreement between the two separate measurement and analysis methods, although the (500 nm, 0.2) film is close. Taken together, the results of Figs. 7 and 8 indicate some aspects of the assumptions or predictions of the analysis section were not observed: the in-plane strains, ε_{11}^{EBSD} and ε_{22}^{EBSD}, in many cases were not identical, and the equality of the measured and predicted distortions, ε_T^{EBSD} and ε_T^{pre}, were not completely independent of the degree of coherence.

5. Discussion

The required elements for a RM, that it be a "material, sufficiently homogeneous and stable with respect to one or more specified properties, which has been established to be fit for its intended use in a measurement process," [37] have been

demonstrated by the prototype RM described. Here, the "measurement process" is accurate EBSD strain measurements, meaning that the EBSD measurements provide an estimate within specifiable uncertainty of true strain quantities. In the case here, the strain quantity was the tetragonal distortion of the $Si_{1-x}Ge_x$ lattice from its unstressed or relaxed state, and the true value of the quantity was established by independent XPS composition and XRD lattice spacing measurements and prior, separate, determinations of $Si_{1-x}Ge_x$ alloy lattice spacings and elastic constants. Quantitative agreement, within calculated experimental uncertainty (Table 1, Fig. 8), between the tetragonal distortion determined from EBSD normal strain component measurements and that from the independent measurements was demonstrated, thus "establishing fit for intended use," as least for those structures that were independently assessed to have epitaxial coherence with the Si substrate. The patterned structures provided easy EBSD access to adjacent Si substrate reference points, further enhancing ease of use and reducing measurement uncertainty. The artifact, in the form of a thin-film patterned chip, is eminently suitable for establishing the RM as "homogeneous and stable with respect to one or more specified properties." The chips are well suited for XPS and XRD, which take about a day/sample for measurement, implying that statistical sampling of chips from a single wafer to establish quantitative bounds on RM initial homogeneity and ongoing stability are easily feasible. Homogeneity and stability were partially demonstrated here through repeated measurements on different width $Si_{1-x}Ge_x$ stripes over the course of a few years, with no significant changes in measurement results. Finally, the XPS and XRD measurements are in principal traceable to SI units *via* explicit use of standard or certified reference materials [38,39] in instrument calibration, thereby providing the most accurate determination of the tetragonal distortion (*via* Eq. (13)). The usefulness of such traceable calibrations for generation of an EBSD strain artifact, however, will depend on materials and instrument operation selections.

Materials selection for an EBSD strain RM formed by a $Si_{1-x}Ge_x$ film on a Si substrate is strongly influenced by the effects of material microstructure. In particular, the reduction of elastic strain energy in the film by the formation of misfit dislocations and reduction in film–substrate lattice coherency [20,21] appears to significantly reduce the correspondence between the tetragonal distortion measured by composition and XRD and by EBSD. Increased Ge fraction and increased film thickness reduced the correspondence here, and yet both are desirable factors in an RM. Increased Ge increases the strain mismatch between the Si lattice and unstrained $Si_{1-x}Ge_x$ alloy (Eqs. (1) and (2)), providing greater strain magnitudes that can therefore be measured with greater relative precision. Increased film thickness decreases the potential convolution of substrate effects with film measurements. Modeling by Winkelmann [40] has shown that the EBSD information depth for Si bombarded with 20 keV electrons, assuming an exponential decay of information with depth, to be about 22 nm. From this depth, the relative contributions of a $Si_{1-x}Ge_x$ film and a Si substrate to EBSD patterns can be calculated; the film contribution is 80% and 90% for film thicknesses of 35 nm and 50 nm, respectively. Similar considerations apply to use of the RM for other strain measurement techniques such as confocal Raman microscopy, for which information depths vary from a few hundred nanometers to over one micrometer [26]. Given that information depth effects appear to only alter the correspondence between measurement techniques when the film microstructure is altered from its pristine state, it is worth considering in more detail how the microstructure of a film develops in terms of the strain energy density dependence on composition and thickness.

The elastic strain energy density (per volume) of the film, $U_{(V)}$, is given by

$$U_V = (1/2)C_{IJ}\varepsilon_I\varepsilon_J,$$

where C_{IJ} are the elastic stiffness constants of the film, ε_I is a component of the strain tensor, contracted notation has been used, and the expression is dual sum over I and J (I, J=1–6). For the system here, $\varepsilon_1=\varepsilon_2=\varepsilon_{11}$ (Eq. (8)), $\varepsilon_3=\varepsilon_{33}$ (Eq. (9)), $C_{11}=C_{22}=C_{33}$, $C_{12}=C_{23}=C_{31}$ and are symmetric. All other ε_I are assumed negligible and thus all other C_{IJ} are irrelevant. Combining these equations into the above gives

$$U_{(V)} = C_{11}(x)\varepsilon_m^2(x)\left(1+\frac{2C_{12}(x)}{C_{11}(x)}\right)\left(1-\frac{C_{12}(x)}{C_{11}(x)}\right)\eta^2.$$

As the out-of-plane dimension of the film is not constrained, it is the elastic strain energy density *per area*, $U_{(A)}=U_{(V)}t$ (t is the film thickness), that is of relevance in terms of minimizing the overall energy of the system (elastic energy+dislocation core energy). Hence,

$$U_{(A)} = C_{11}(x)\varepsilon_m^2(x)f(x)t\eta^2 \tag{15}$$

and is seen to be the product of the first three terms that depend only on film material properties *via* composition x; the characteristic modulus, C_{11}, the in-plane mismatch strain, ε_m, and a weakly-varying term that accounts for out-of-plane strain, f (≈ 1.1 here); a fourth term that characterizes the film geometry *via* thickness, t; and a final term that characterizes the microstructure of the film–substrate system, the degree of coherence, η. Inverting Eq. (15) provides some insight into how film microstructure develops and the considerations for selecting a material for a RM:

$$\eta = \left[\frac{U_{(A)}}{C_{11}(x)\varepsilon_m^2(x)f(x)t}\right]^{1/2} = \left[\frac{U_{(A)}}{U_{(A)}^{max}}\right]^{1/2}, \tag{16}$$

where the denominator in the first line of Eq. (16) is recognized as the maximum (areal) strain energy density possible in the film, $U_{(A)}^{max}$. Eq. (16) provides a physical interpretation of η: the ratio of (remnant strain energy density of a film in a state of partial coherence)/(maximum possible energy density before the loss of any coherence). Alternatively, Eq. (16) suggests a testable hypothesis for the nature of the films and the prediction of η: The remnant areal strain energy density of the films, $U_{(A)}$, is a constant. Fig. 9 is a plot of η against $U_{(A)}^{max}$ (calculated from the values in Table 1 and Eq. (16)) in logarithmic coordinates. The solid

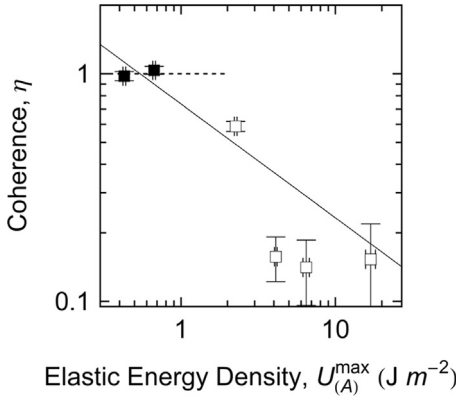

Fig. 9. Plot of coherence of $Si_{1-x}Ge_x$ films on Si substrates *vs.* the maximum elastic strain energy density of a film. Data and error bars are from Table 1. Filled squares represent "coherent films" shown in Fig. 5; open squares represent "incoherent films" shown in Fig. 6. The solid line indicates invariant remnant elastic strain energy density on partial loss of coherence.

line in Fig. 9 is of slope −1/2, consistent with the hypothesis, and describes the observations. The implication is that in this system the films formed misfit dislocations to reduce the elastic strain energy density to the constant value, $U_{(A)}$, and thus the coherence of the film–substrate system, until it was energetically unfavorable to form another dislocation (*e.g.*, the dislocation core energy created was greater than the elastic strain energy released).

Film microstructure development as a function of the (t, x) doublet is thus mapped out in the coordinates of Fig. 9. For very small values of (t, x), such that $U_{(A)}^{max}$ is small, the film remains coherent with the substrate and the film remains unrelaxed. As (t, x) increases the film travels along the $\eta=1$ trajectory, the dashed line in Fig. 9, as $U_{(A)} = U_{(A)}^{max}$ increases. Eventually, the elastic strain energy density in the film reaches a critical value, at a critical combination of (t, x), and the first misfit dislocations are initiated, with conditions specified by the Mathews–Blakeslee equilibrium criterion [41], or, more likely for the films here, by kinetic criteria as specified by Houghton [21], at the intersection of the dashed and solid lines in Fig. 9. Further increases in (t, x) lead to the initiation of more and more misfit dislocations and greater loss of coherence, and the film travels along the $U_{(A)}$ fixed-η decreasing trajectory, the solid line of slope −1/2 in Fig. 9. As noted above, EBSD measurements are restricted to the top few tens of nanometers of a film with a similar spot size, whereas XRD measures the entire film thickness with a spot size of millimeters. For correspondence between strain measurements by the two techniques, the strain state and microstructure of the surface must be identical to that of the bulk, and a *perfectly* coherent film meets these criteria. Consideration of quoted (t, x) values in prior works [9,10,14,22,23] and use of Eq. (16) gives $U_{(A)}^{max}$ values for $Si_{1-x}Ge_x$ films in these works in the range (0.01–1.5) J m^{-2} (using the smallest t values from [9,22]). This range suggests from Fig. 9 that near coherent films were studied in these works, consistent with the agreement observed between HR-EBSD strain measurements and XRD [9,14] and FEA [10]. Trajectories such as those in Fig. 9 provide guidance for selecting film (t, x) such that $\eta=1$. However, Fig. 8 suggests that at least some partially coherent films might also meet the criteria of experimentally indistinguishable strain state and microstructure for the surface and bulk and the trajectories of Fig. 9 can provide upper bounds for (t, x) to achieve the required minimum values of η.

Finally, some consideration needs to be given to SEM instrument hardware, operational parameters, and EBSP analysis methods in using the RM. Preliminary explorations suggest the following require greater experimentation and analysis to assess and improve the accuracy and precision of EBSD for strain measurement. From a hardware perspective, EBSD detectors in SEMs are known to produce distortions in EBSPs that can affect inferred strains. The principal of these distortions are barrel distortion and a phosphor effect and these have been discussed by Britton et al. [11,12] and Mingard et al. [17]. Barrel distortion of the pattern detection system is typically quantified before a detector is installed; the effects can be reduced to less than the strain variations observed here. The microstructure of the phosphor causes the phosphor efficiency to vary spatially and can result in a faint residual image of the phosphor in the EBSPs that is incompletely removed by background subtraction. In preliminary work, it has been found that the size of the phosphor effect is greatest in pattern areas where the signal-to-noise ratio is low and is greater for smaller ROIs. It has been found that the phosphor effect can be significantly reduced by increasing the SEM probe current; in addition it is important that the EBSP is well centered. These considerations will be the subject of further systematic study. SEM accelerating voltage affects the strains inferred largely through information depth effects in films of partial or zero coherence.

An additional consideration is measurement precision. The precision stated in the introduction is for sequential measurements within a stripe or gap and are essentially a “noise floor”; expanded estimates of uncertainty including re-mounting and alignment effects are required to establish a better estimate of repeatability precision. Two critical parameters in the analysis methodology that affect strain estimation are the selection of ROI positions in the EBSP and application of the band-pass filter prior to cross correlation of the ROIs; detailed measurements of the effects of changes in these parameters are required to provide better estimates of both precision and accuracy. Sensitivity of strain estimation to ROI position selection may be due to magnetic and (perhaps) electric field effects within the SEM, and hence should be assessed on various SEMs.

The above instrument, operational, and analysis issues will be the focus of future work. Additionally, EBSD measurements can be compared with those from atomic force microscopy, high resolution XRD, confocal Raman microscopy, and analytical and numerical modeling [27] to further refine the precision and accuracy of HR-EBSD strain mapping.

6. Conclusions

Results have been presented that strongly support the viability of patterned $Si_{1-x}Ge_x$ thin film structures, heteroepitaxially deposited on Si substrates, as RM artifacts to establish the accuracy of HR-EBSD strain measurement methods. Independent XRD measurements of film lattice spacing, in concert with XPS composition measurements, provided a measure of film–substrate epitaxial coherence and a prediction of epitaxial strain that was directly testable by EBSD measurements. Films that were assessed to be coherent with the substrate (thin films of moderate Ge composition) exhibited identical strain values when measured by EBSD and XRD, within relative experimental uncertainty of order 2%, and thus provide suitable prototypes for a strain RM. EBSD can be used as an accurate quantitative microscopy method for mapping strains, as demonstrated in line scans across $Si_{1-x}Ge_x$ stripes on Si substrate gaps with about 1 μm step size. Considerations of film coherence and maximum elastic strain energy density suggest that films converge to a common, reduced strain energy density on loss of coherence and that the coherence-maximum energy density trajectory provides a guideline for film composition and thickness selection in RM development; it is unclear that fully coherent films are necessary for a strain RM. A full instrument and analysis sensitivity assessment is required before specification of final RM precision and accuracy.

References

[1] S.I. Wright, M.M. Nowell, D.P. Field, Microsc. Microanal. 17 (2011) 316.
[2] A.J. Wilkinson, T.B. Britton, Mater. Today 15 (2012) 366.
[3] J. Li, Z. Shan, E. Ma, MRS Bull. 39 (2014) 108.
[4] M. Marzencki, M. Defosseux, S. Basrour, J. Microelectromech. Syst. 18 (2009) 1444.
[5] M.L. Lee, E.A. Fitzgerald, M.T. Bulsara, M.T. Currie, A. Lochtefeld, J. Appl. Phys. 97 (2005) 011101.
[6] J.S. Hwang, A. Gokarna, Y.-H. Cho, J.K. Son, S.N. Lee, T. Sakong, H.S. Paek, O.H. Nam, Y. Park, S.H. Park, J. Appl. Phys. 102 (2007) 013508.
[7] V.T. Srikar, A.K. Swan, M. Selim Ünlü, B.B. Goldberg, S.M. Spearing, J. Microelectromech. Syst. 12 (2003) 779.
[8] J.A. Howell, M.D. Vaudin, R.F. Cook, J. Mater. Sci. 49 (2014) 2213.
[9] A.J. Wilkinson, Ultramicroscopy 62 (1996) 237;
A.J. Wilkinson, Mater. Sci. Technol. 13 (1997) 79.
[10] S. Villert, C. Maurice, C. Wyon, R. Fortunier, J. Microsc. 223 (2009) 290.
[11] T.B. Britton, J. Jiang, R. Clough, E. Tarleton, A.I. Kirkland, A.J. Wilkinson, Ultramicroscopy 135 (2013) 126.
[12] T.B. Britton, J. Jiang, R. Clough, E. Tarleton, A.I. Kirkland, A.J. Wilkinson, Ultramicroscopy 135 (2013) 136.
[13] A.J. Wilkinson, G. Meaden, D.J. Dingley, Ultramicroscopy 106 (2006) 307.

[14] K.Z. Troost, P. van der Sluis, D.J. Gravesteijn, Appl. Phys. Lett. 62 (1993) 1110.
[15] D.K. Bowen, J. Bradler, S. Newstead, Personal communication as cited in Wilkinson, 1996 and 1997 ,1995.
[16] A.J. Wilkinson, G. Meaden, D.J. Dingley, Mater. Sci. Technol. 22 (2006) 1271.
[17] K. Mingard, A. Day, C. Maurice, P. Quested, Ultramicroscopy 111 (2011) 320.
[18] A. Belsky, M. Hellenbrandt, V.L. Karen, P. Luksch, Acta Crystallogr. B 58 (2002) 364.
[19] J.P. Dismukes, L. Ekstrom, R.J. Paff, J. Phys. Chem. 68 (1964) 3021.
[20] D.C. Houghton, C.J. Gibbings, C.G. Tuppen, M.H. Lyon, M.A.G. Halliwell, Appl. Phys. Lett. 56 (1990) 460.
[21] D.C. Houghton, J. Appl. Phys. 70 (1991) 2136.
[22] A.J. Wilkinson, J. Electron Microsc. 49 (2000) 299.
[23] A.J. Wilkinson, Appl. Phys. Lett. 89 (2006) 241910;
A.J. Wilkinson, G. Meaden, D.J. Dingley, Superlattices Microstruct. 45 (2009) 285.
[24] M.A.G. Halliwell, M.H. Lyons, S.T. Davey, M. Hockly, C.G. Tuppen, Semicond. Sci. Technol. 4 (1989) 10.
[25] L.H. Wong, C.C. Wong, J.P. Liu, D.K. Sohn, L. Chan, L.C. Hsia, H. Zang, Z.H. Ni, Z.X. Shen, Jpn. J. Appl. Phys. 44 (2005) 7922.
[26] M.D. Vaudin, Y.B. Gerbig, S.J. Stranick, R.F. Cook, Appl. Phys. Lett. 93 (2008) 193116.
[27] M.D. Vaudin, G. Stan, Y.B. Gerbig, R.F. Cook, Ultramicroscopy 111 (2011) 1206.
[28] C.E. Murray, A.J. Ying, S.M. Polvino, I.C. Noyan, Z. Cai, Powder Diffr. 25 (2010) 108.
[29] T. Tezuka, N. Sugiyama, T. sa Mizuno, S.-I. Takagi, VLSI Tech. Dig. (2002) 96. http://dx.doi.org/10.1109/VLSIT.2002.1015405.
[30] P. Ganster, A. Saul, G. Treglia, arXiv:1207.7238 [cond-mat.mtrl-sci] (accessed 11.07.14).
[31] H.H. Richter, A. Wolff, B. Tillack, T. Skaloud, Mater. Sci. Eng. B 27 (1994) 39.
[32] Certain commercial equipment, instruments, or materials are identified in this paper to foster understanding. Such identification does not imply recommendation or endorsement by the National Institute of Standards and Technology, nor does it imply that the materials or equipment identified are necessarily the best available for the purpose.
[33] International Standard ISO 18118, 2004.
[34] H.J. McSkimin, P. Andreatch, J. Appl. Phys. 34 (1963) 651.
[35] H.J. McSkimin, P. Andreatch, J. Appl. Phys. 35 (1964) 2161.
[36] J.M. Gorham, T. Nguyen, C. Bernard, D. Stanley, R.D. Holbrook, Surf. Interface Anal. 44 (2012) 1572.
[37] ⟨http://www.nist.gov/srm/definitions.cfm⟩ (accessed 23.06.14).
[38] M.D. Vaudin, E.G. Kessler, D.M. Owen, Metrologia 48 (2011) 201.
[39] ⟨https://www-s.nist.gov/srmors/view_cert.cfm?srm=2000⟩ (accessed 23.06.14).
[40] A. Winkelmann, F. Savat-Pujol, W.S.M. Werner, Microsc. Microanal. 19 (2013) 738.
[41] J.W. Matthews, A.F. Blakeslee, J. Cryst. Growth 27 (1974) 118.